Acta Materialia 246 (2023) 118713

Contents lists available at ScienceDirect

Acta Materialia

journal homepage: www.elsevier.com/locate/actamat

Full length article

Solidification modes during additive manufacturing of steel revealed by high-speed X-ray diffraction

Hans-Henrik König [a], Niklas Holländer Pettersson [a], A. Durga [a,1], Steven Van Petegem [b,*], Daniel Grolimund [c], Andrew Chihpin Chuang [d], Qilin Guo [e], Lianyi Chen [e], Christos Oikonomou [f], Fan Zhang [g,*], Greta Lindwall [a,*]

[a] KTH Royal Institute of Technology, Brinellvägen 23, Stockholm SE-10044, Sweden
[b] Structure and Mechanics of Advanced Materials, Paul Scherrer Institute, PSI, Forschungsstrasse 111, Villigen CH-5232, Switzerland
[c] MicroXAS Beamline, Paul Scherrer Institute, PSI, Forschungsstrasse 111, Villigen CH-5232, Switzerland
[d] X-Ray Science Division, Advanced Photon Source, Argonne National Laboratory, Lemont, IL 60559, USA
[e] Department of Mechanical Engineering, University of Wisconsin-Madison, Madison, WI 53706, USA
[f] Uddeholms AB, Uvedsvägen, Hagfors SE-68333, Sweden
[g] Material Measurement Laboratory, National Institute of Standards and Technology, 100 Bureau Drive, Gaithersburg, MD 20899, USA

ARTICLE INFO

Keywords:
Solidification
Synchrotron X-ray diffraction
Additive manufacturing
Powder bed fusion
Steel

ABSTRACT

Solidification during fusion-based additive manufacturing (AM) is characterized by high solidification velocities and large thermal gradients, two factors that control the solidification mode of metals and alloys. Using two synchrotron-based, *in situ* setups, we perform high-speed X-ray diffraction measurements to investigate the impact of the solidification velocities and thermal gradients on the solidification mode of a hot-work tool steel over a wide range of thermal conditions of relevance to AM of metals. The solidification mode of primary δ-ferrite is observed at a cooling rate of 2.12×10^4 K/s, and at a higher cooling rate of 1.5×10^6 K/s, δ-ferrite is suppressed, and primary austenite is observed. The experimental thermal conditions are evaluated and linked to a Kurz-Giovanola-Trivedi (KGT) based solidification model. The modelling results show that the predictions from the multicomponent KGT model agree with the experimental observations. This work highlights the role of *in situ* XRD measurements for a fundamental understanding of the microstructure evolution during AM and for validation of computational thermodynamics and kinetics models, facilitating parameter and alloy development for AM processes.

1. Introduction

Additive manufacturing (AM) of metals, or metal 3D printing, has attracted increasing attention due to the geometrical design freedom, allowing for new, previously unimaginable applications of metallic materials [1]. Furthermore, AM processing often introduces unique microstructures [2,3]. The most common metal AM technology is based on melting and subsequent solidification of metal powder layers using a laser energy source, i.e., laser powder bed fusion (L-PBF), where metallic components are created layer-by-layer from the powder feedstock [4]. The high laser scanning speeds create comparable small melt pools that solidify rapidly resulting in solidification structures governed by highly transient solidification conditions [1].

Solidification is an extensively studied topic, and decades of research have advanced our fundamental understanding of solidification through both, the development of rigorous analytical models and accurate numerical approaches, e.g., [5–7], and the access to sophisticated experimental techniques, e.g., [8–10]. Solidification is one of the most critical processing steps for metals and alloys, and advances within the field have been crucial for the design of new metallic materials and innovative metallurgical processes such as metal AM. Independently of the process, the resulting solidification structure is determined by the molten region shape and the specific conditions at the liquid-solid interface represented by the local thermal gradient (G) and the solidification interface velocity (V) [11]. The ability to steer these conditions through process specifics and alloying enables localized control of the

* Corresponding authors.
E-mail addresses: steven.vanpetegem@psi.ch (S. Van Petegem), fan.zhang@nist.gov (F. Zhang), gretal@kth.se (G. Lindwall).
[1] Present address: Department of Metallurgical Engineering and Materials Science, Indian Institute of Technology Bombay, Mumbai, 400076, India.

https://doi.org/10.1016/j.actamat.2023.118713
Received 29 June 2022; Received in revised form 8 December 2022; Accepted 18 January 2023
Available online 19 January 2023

Table 1
Nominal composition of the steel powder in mass-%.

Element	Fe	C	Cr	Mo	V	Mn	Si	N
Composition [mass-%]	Bal.	0.35	4.93	2.24	0.54	0.45	0.25	0.049

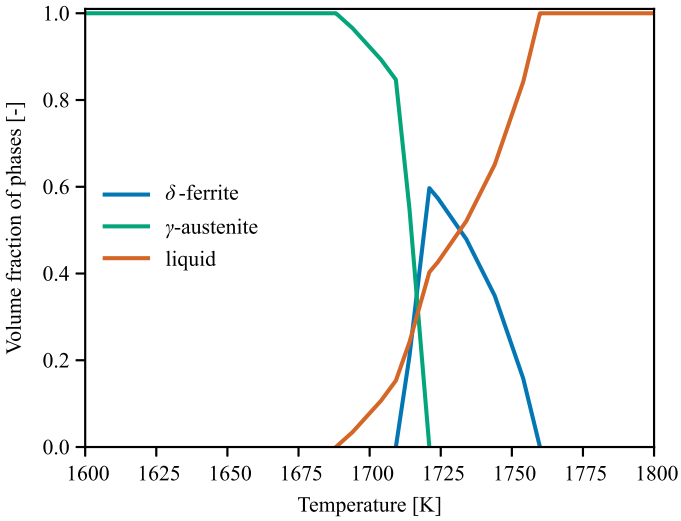

Fig. 1. Calculated equilibrium phase fractions of the studied material in the temperature range 1400 K to 1800 K showing that δ-ferrite is the primary solidification phase at equilibrium conditions.

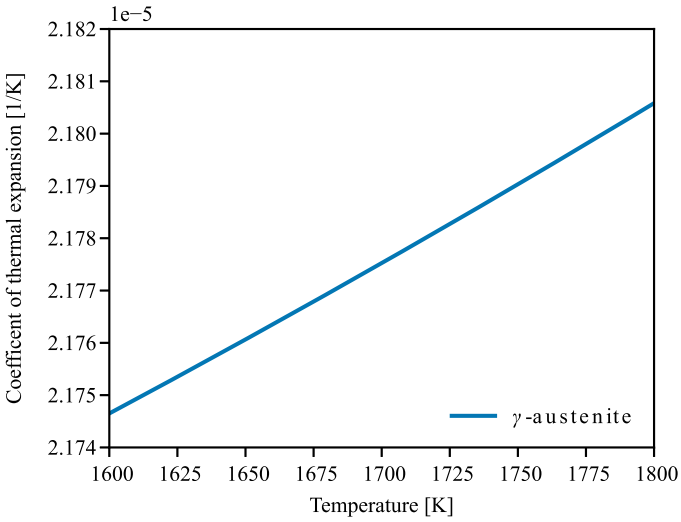

Fig. 2. Coefficient of thermal expansion of γ from 1400 K to 1800 K.

microstructure and is instrumental in the current development of AM [12,13]. For conventional metallurgical processes, solidification can often be described by assuming local equilibrium at the solidification front (the phase boundary) between the liquid and solid phases [14]. However, at the high solidification velocities typical for the AM processes, deviation from such a local-equilibrium assumption is expected [3].

The transition from equilibrium to non-equilibrium solidification can be treated as a function of V and G, and it has been shown that, with increasing V, the elemental partitioning deviates from the equilibrium value (solute trapping), and the liquid-solid interface morphology changes [15]. In addition, the primary solidification of a metastable phase may occur [8]. This is of technical importance for L-PBF processing of austenitic or martensitic steels as it has been shown in the welding literature that higher solidification velocities may alter the solidification mode [9,16] and suppress the δ-ferrite formation, impacting the hot cracking susceptibility [17,18] or the mechanical properties of steel welds [19]. Since the AM process resembles the solidification events typical for laser welding [1], the fundamental principles controlling the solidification microstructure during welding are also relevant for AM. However, the question arises as to what extent we can leverage existing solidification models developed for laser melting and welding to predict the microstructure evolution during AM.

Previously, Chou et al. [20] studied the solidification structure in an L-PBF processed hot-work tool steel and applied the Kurz-Giovanola-Trivedi (KGT) [15] solidification model for laser melting [17] and welding [8,17] to calculate the dendrite tip temperatures for δ-ferrite and austenite (γ) under L-PBF conditions. The calculations showed that at higher solidification velocities, in the range expected during L-PBF, γ may have a higher tip temperature and, therefore, a higher driving force to form as the primary solidification phase compared to δ-ferrite, which is the primary solidification phase if local equilibrium holds at the liquid-solid interface [20]. The results were compared with a microstructural characterization of the as-built material, which showed no signs of δ-ferrite. However, the inference about the solidification mode during AM from post-process microstructure characterization of the as-built material is limited. Instead, synchrotron *in situ* X-ray measurements that allow for recording of the microstructure evolution during AM with high temporal (several MHz [21]) and spatial resolution (1 μm [22]) can address these phenomena [23]. Several synchrotron sample environments for *in situ* and *in operando* X-ray imaging and diffraction during AM have been developed and successfully implemented [24–31] to study, e.g., melt pool dynamics [32,33], pore [33,34] and crack evolution [35,36], phase transformations [30,37], stress evolution [38,39] and thermal conditions [40,41].

In the present study, we utilize two different *in situ* L-PBF sample environments implemented at synchrotron beamlines at the Swiss Light Source (SLS), Switzerland [27] and at the Advanced Photon Source (APS), USA [24], to understand the solidification modes of a hot-work tool steel under two processing conditions. The goal is to elucidate the solidification mode, focusing on the change of the solidification mode from primary δ-ferrite to primary γ with increasing solidification velocity. The experimental results are compared to calculations based on the KGT solidification model, utilizing an analytical thermal model to link measured cooling rates with thermal conditions at the melt pool scale.

2. Methods

2.1. Material

The material studied in this work is a martensitic hot-work tool steel with the composition listed in Table 1. The equilibrium phase fractions of this composition are calculated using the Thermo-Calc Software package [42] employing the Thermo-Calc Software TCFE Steels/Fe-alloys database version 11 [43] (Fig. 1) for a temperature range from 1400 K to 1800 K, which is relevant for the solidification observations. The equilibrium phases in this temperature range are liquid, δ-ferrite (bcc) and γ-austenite (fcc), suggesting that during solidification where local interface equilibrium is valid, the solidification mode is primary δ-ferrite. The liquidus temperature is $\approx$ 1760 K.

To evaluate the thermal expansion effect of the γ phase, the coefficient of thermal expansion (CTE) in the temperature range of 1400 K and

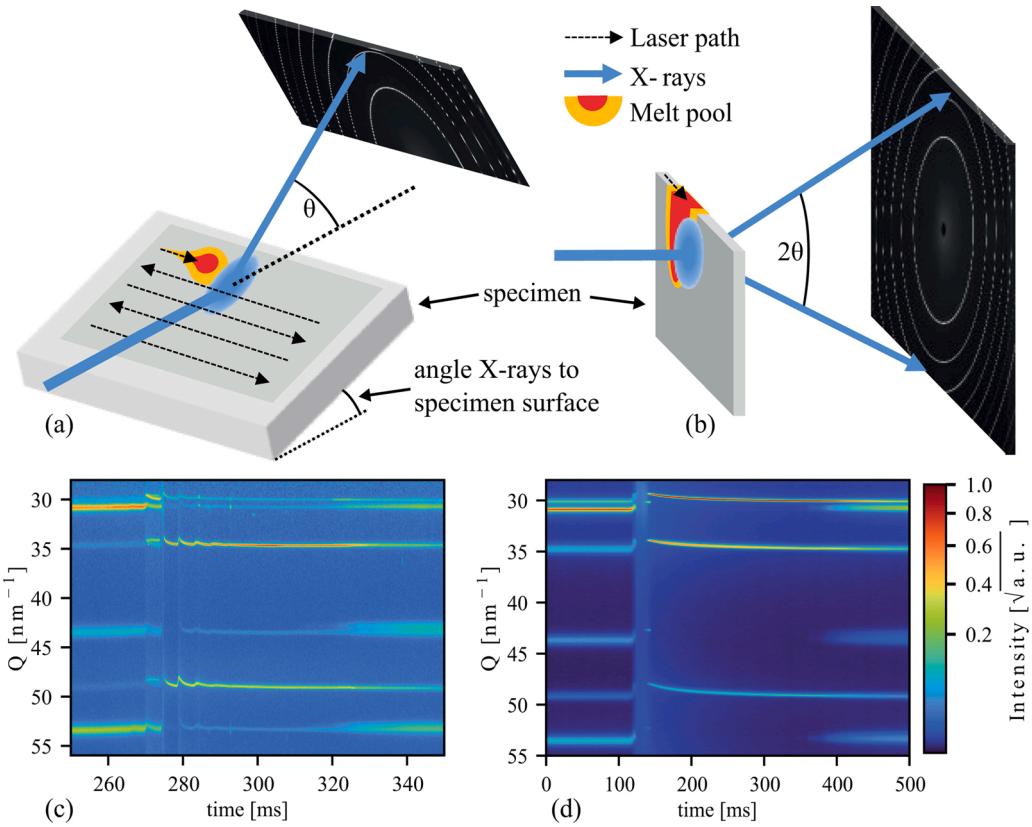

Fig. 3. Schematics of the experimental setups, (a) reflection mode, (b) transmission mode, (c) stacked diffraction pattern over time during printing in reflection mode in MiniSLM (20,000 Hz), (d) stacked diffraction pattern over time during printing in transmission mode in AM-replicator (250 Hz).

Table 2
Input parameters for the KGT model.

Parameter	Value
Solute diffusivity for all elements, D	5×10^{-9} m^2/s
Characteristic diffusion distance, a_0	5×10^{-9} m
Interface kinetic coefficient, μ	10 m/s/K
Liquidus temperature austenite, T_{liq}	1749.3 K
Gibbs-Thompson coefficient austenite, Γ	5.6×10^{-8} m•K
Liquidus temperature δ-ferrite, T_{liq}	1758.4 K
Gibbs-Thompson coefficient δ-ferrite, Γ	5.5×10^{-8} m•K
Velocity-dependent partition coefficient, k_v^i	Calculated with the model by Aziz [56] and material-specific Calphad thermodynamic database at every iteration.
Liquidus slopes, m_v^i	Calculated with the model by Aziz [56] and material-specific Calphad thermodynamic database at every iteration.

1800 K was calculated using the Thermo-Calc Software TCFE Steels/Fe-alloys database version 11 [43] (Fig. 2). Within this temperature range, the change in CTE is subtle (≈ 0.5 %) and the CTE can be reasonably approximated as constant (CTE = 2.18×10^{-5} K^{-1}) at liquidus temperature.

Different specimens were used for the *in situ* XRD experiments depending on the sample environments. A nitrogen-atomized powder feedstock was used for the experiments at SLS. This powder was sieved to 20–50 μm size fraction and used to additively manufacture miniature builds on a build plate manufactured from a soft annealed version of the same alloy. For the APS experiments, an EOS M290 was used to fabricate a cuboid with dimensions of 9 mm × 11 mm × 54 mm from the same starting powders. From this cuboid, thin plates of dimensions 0.5 mm × 3 mm × 40 mm were extracted with electrical discharge machining. The plate surfaces had a 1200 grit finish using SiC paper before the laser melting experiment.

2.2. *In situ* X-ray diffraction measurements

The two sample environments utilized to study the solidification behaviour of the hot-work tool steel at varying AM solidification conditions using *in situ* XRD are shown schematically in Fig. 3. The AM-Replicator [24] setup was used at the 1-ID-E beamline at APS for transmission mode measurements during laser melting of a thin plate specimen (see Fig. 3(b)). The MiniSLM was used at the micro-XAS beamline at the SLS for reflection mode measurements (Fig. 3(a)) on a multilayer cuboid geometry. Further details on the MiniSLM sample environment can be found in previous works by Hocine et al. [27,44].

With the AM-Replicator, XRD data were recorded before, during and after laser melting. A single laser track was scanned on the 0.5 × 40 mm side of the plate with a laser power of 218 W, a scan speed of ≈ 0.05 m/s, a $1/e^2$ laser beam size of 100 μm, and a wavelength of 1070 nm. The 2D diffraction patterns were acquired using a PILATUS3X-2M CdTe X-ray detector (DECTRIS, Switzerland) at a frame rate of 250 Hz and with an exposure time of 3 ms per frame. The X-ray beam size was 50 μm × 30 μm (horizontal × vertical), where the beam was focused vertically to FWHM of ≈ 30 μm by a Silicon sawtooth lens and slit down horizontally to 50 μm. This resulted in an interaction volume of the X-ray beam with the sample (spatial resolution) of 50 μm x 30 μm (FWHM) x 500 μm in the transmission mode measurements. The X-ray energy was 61.332 keV calibrated by Ytterbium foil.

The sample geometry investigated with the MiniSLM in reflection

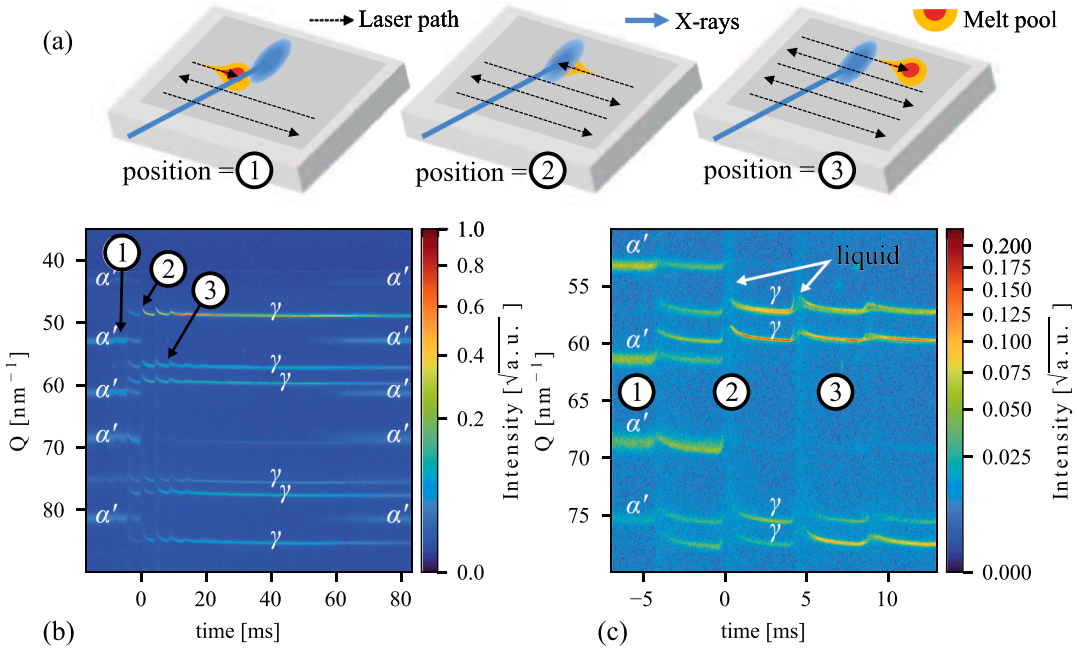

Fig. 4. Schematic of the reflection mode measurement, and diffraction heat maps with a recording rate of 40 000 Hz (MiniSLM) showing the phase transformations over time, (a) positional relation of the X-ray beam and laser at different times, (b) transformations during 100 ms, (c) signal during laser-matter interaction including the liquid state signal, that indicates measurement of a completely liquified melt pool (0 ms, position=2).

mode was an 8 mm × 2 mm cuboid (snake hatching, 80 µm hatch distance) of 12 layers with a layer thickness of 30 µm. The laser power applied at SLS was 300 W, the scanning speed was 0.6 m/s, the $1/e^2$ laser beam size was 50 µm, and the wavelength was 1070 nm. 2D X-ray diffraction patterns were acquired with an EIGER1M detector developed at PSI [45]. This detector consists of 2 modules, each containing 500 000 pixels with a size of 75 × 75 µm, resulting in a total active area of approximately 8 × 8 cm^2. The experiments were performed at frame rates of 20 kHz or 40 kHz, with an exposure time of 45 µs and 20 µs per frame, respectively. The incident X-ray energy was 17.2 keV and the focused beam size was 80 µm × 35 µm size. The X-ray's incident angle was 18°, leading to an illuminated footprint of 80 µm × 113 µm (horizontal × vertical) on the sample surface. The effective penetration depth [46] during the reflection mode measurements was a few tens of micrometers with a mass attenuation coefficient of 3500.94 cm^2/g [47] of the sample composition (see Table 1). For the investigated signals in the q-range of 30 nm^{-1} to 50 nm^{-1} the effective penetration depth was 57 ± 37 µm. This resulted in an interaction volume of the X-ray beam with the sample (spatial resolution) of 80 µm x 130 µm x 57 ± 37 µm in the reflection mode measurements. These measurement settings allowed for sampling of a single melt pool. Between the consecutive manufacturing of built layers, a ≈ 10 min adjustment period allowed the sample to cool down to close to room temperature.

2.3. Diffraction data

2.3.1. Integration and peak fitting

The normalized XRD data were first integrated following standard procedures established at the beamlines. Second, peak-profile analysis was performed on the XRD data to acquire the peak positions. The data recorded with the MiniSLM was adjusted to account for layer shrinking during laser melting (Appendix A).

The 2D diffraction patterns were azimuthally integrated using Fit2D [48] and pyFAI [49] for the data from AM-Replicator and MiniSLM measurements, respectively. Here, the δ-ferrite has a body-centred-cubic (bcc) unit cell, and the austenite γ has a face-centred-cubic (fcc) unit cell. The peaks were fitted applying the PseudoVoigt model from the Python library lmfit [50] on the peaks in the data corresponding to the {110}, {200}, and {211} peaks of the bcc and the {111}, {200}, and {220} peaks of the fcc, to obtain the respective peak positions. An example of a typical integrated XRD line profile, the performed peak fit, and the residuals are shown in Appendix B for the AM-Replicator and the MiniSLM data, respectively.

2.3.2. Cooling rates

The cooling rates ($\dot{T}$) were determined following the change of the diffraction peak positions during the experiments. The lattice parameter (a) was calculated using the three γ peaks ({111}, {200}, {220}) by applying Bragg's law for cubic systems,

$$a = \frac{\lambda\sqrt{h^2 + k^2 + l^2}}{2\sin(\Theta)} \tag{1}$$

where λ is the X-ray wavelength, Θ is one half of the diffraction angle 2Θ, and h, k and l are the Miller indices of the respective set of lattice planes.

To account for the convolution of the cooling of the probed locations within the X-ray interaction volume, the time-dependent lattice parameter is fitted by an exponential decay function with two exponential terms using the Python library lmfit [50],

$$a(t) = A\cdot\exp\left(-\frac{t}{\tau_1}\right) + B\cdot\exp\left(-\frac{t}{\tau_2}\right) + a_0 \tag{2}$$

where t is the time, A and B are the initial amplitudes, τ_1 and τ_2 are the rate constants and a_0 is the lattice parameter of the first solid detected after liquid. The obtained parameters from fitting Eq. (2) to the data, were used to evaluate the derivative of the lattice parameter $\dot{a}(t)$. Together with the coefficient of thermal expansion CTE, $\dot{a}(t)$ was used to obtain the cooling rate utilizing the following expression:

$$\dot{T}(t) = \frac{\dot{a}(t)}{CTE\cdot a_0} \tag{3}$$

Here, the constant CTE value of 2.18 × 10^{-5} K^{-1} was used for the alloy composition at 1750 K (Fig. 2).

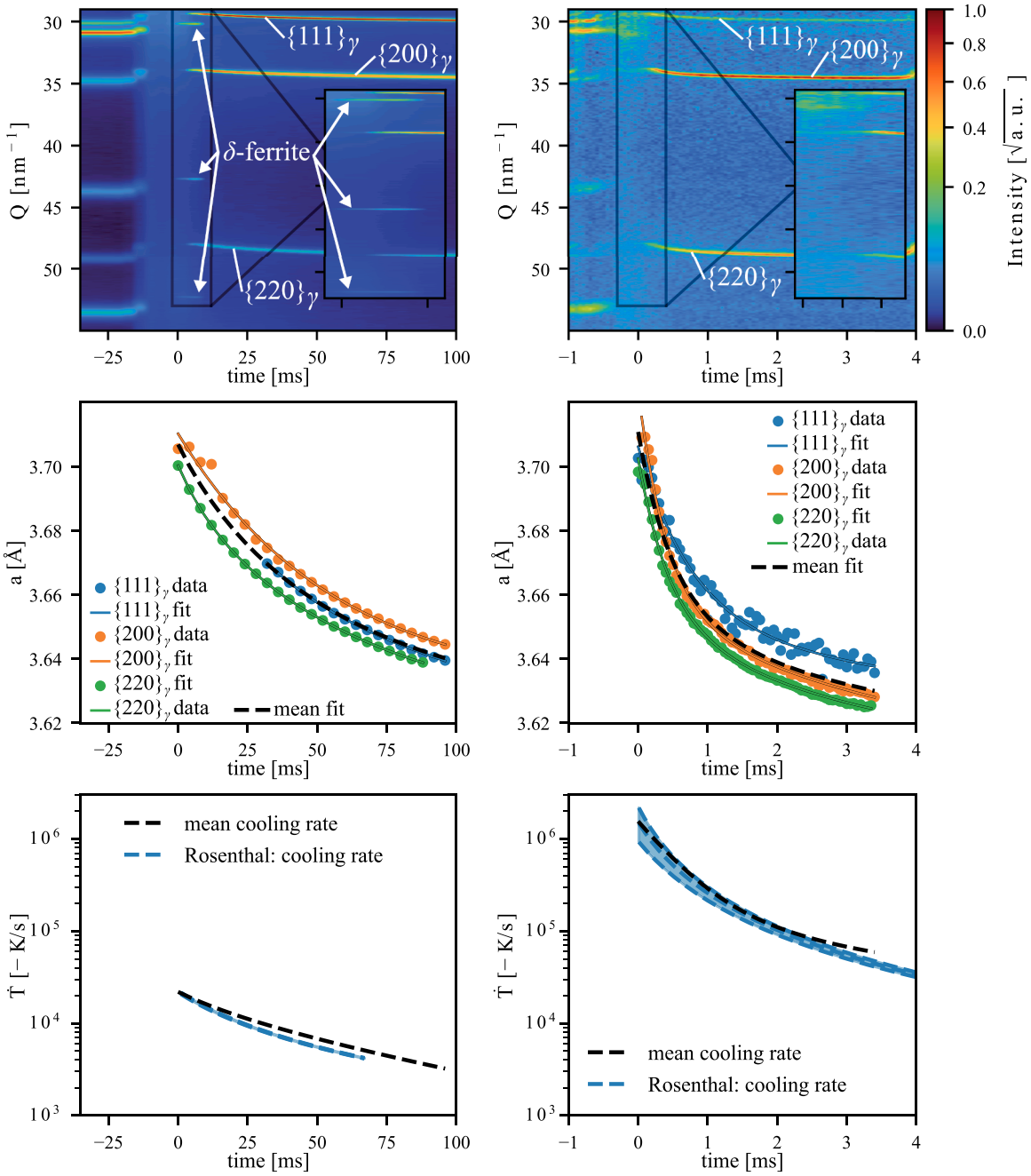

Fig. 5. Diffraction heat maps of the solidification in the (a) AM-Replicator (250 Hz) and (b) MiniSLM (20,000 Hz), (c) and (d) lattice parameter of the γ phase during solidification, (e) and (f) cooling rates during solidification obtained from γ lattice parameter change and calculated cooling rates.

Table 3
Mean thermal conditions ± range within the X-ray interaction volume for AM-Replicator and MiniSLM conditions, cooling rate Ṫ, thermal gradient G, solidification velocity V, obtained during the first 1 ms of solidification.

	AM-Replicator	MiniSLM
Cooling rate (mean), $\dot{T}$ [K/s]	$2.12 \bullet 10^4 \pm 0.04 \bullet 10^4$	$1.5 \bullet 10^6 \pm 0.7 \bullet 10^6$
Thermal gradient (mean), G [K/m]	$4.4 \bullet 10^5 \pm 0.2 \bullet 10^5$	$5 \bullet 10^6 \pm 3 \bullet 10^6$
Solidification velocity (mean), V [m/s]	0.048 ± 0.002	0.32 ± 0.2

2.4. Thermal modelling and phase selection

To compare the experimental results to the solidification tip temperature model, the thermal profiles of line scans of a laser on the sample geometries were calculated using the Rosenthal equation [51]. The Rosenthal equation solves the heat conduction of a point heat source traversing an infinite substrate in x-direction with scanning speed v neglecting heat convection and radiation in three dimensions [52],

$$T(x,r) = T_0 + \frac{aQ}{2\pi kr}\exp\left\{-\frac{v}{2\alpha}(r + x_{rel})\right\} \quad (4)$$

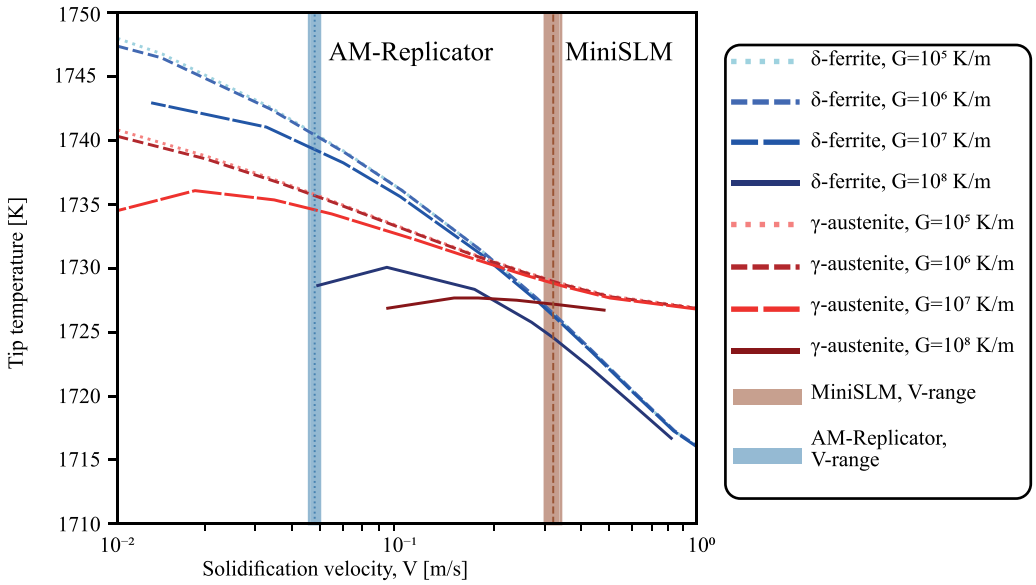

Fig. 6. Calculated tip temperatures of δ-ferrite and γ for the thermal gradients 10^5 K/m, 10^6 K/m, 10^7 K/m and 10^8 K/m versus solidification velocity. At the solidification velocity ranges of the X-ray interaction volume of the AM-Replicator (blue vertical band) and the MiniSLM (red vertical band), the primary solid phases are γ and δ-ferrite, respectively. (For interpretation of the references to colour in this figure legend, the reader is referred to the web version of this article.).

where T_0 is the initial temperature, a is the absorptivity, Q is the power, k is the thermal conductivity, α is the thermal diffusivity, v is the scanning speed, $x_{rel} = x - vt$ is the x-coordinate relative to the heat source and $r = \sqrt{x_{rel}^2 + y_{rel}^2 + z_{rel}^2}$ is the distance to the heat source. The thermal diffusivity is given as $\alpha = \rho c_p / 2k$, where ρ is the density, and c_p is the specific heat capacity of the substrate. To calculate the thermal conditions of the plate specimen, the modified Rosenthal equation for thin wall was used [53],

$$T = T_0 + \frac{n\,Q}{\pi\,k\,b}\,exp\left(\frac{-Vx_{rel}}{2\alpha}\right)K_0\left(\frac{Vr}{2\alpha}\right) \quad (5)$$

where b is the wall thickness, K_0 is the modified Bessel function of the second kind and order zero and $r = \sqrt{x_{rel}^2 + z_{rel}^2}$. To obtain the cooling rate $\dot{T}$ the derivative of the temperature with respect to time $\dot{T} = \partial T / \partial t$ was calculated. The thermal gradient G was calculated with $G = |\nabla T|$ [53]. And the solidification velocity V was determined as $V = T / G$ [53].

For the MiniSLM the thermal profile on an infinite plate was calculated utilizing Eq. (4). For the plate geometry used in the AM-Replicator, a thin-wall approximation of the Rosenthal equation was implemented (Eq. (5)). The following input parameters were used, an absorptivity of 0.55 [54], a thermal conductivity of 32 W/m/K [55], a specific heat capacity of 695 J/kg/K [43] and a density of 7.51 kg/m^3 [43]. The calculations were used to predict the thermal gradient G, the solidification velocity V, and the resulting cooling rate $\dot{T}$. For comparison with the experimental data, the calculations were performed for calculation domains of the same dimension as the X-ray interaction volumes (see Section 2.2). Within these domains only grid points that exhibited a temperature below the liquidus temperature (1760 K) of the sample material were used to obtain G, V, and $\dot{T}$. This procedure ensured comparability between calculated and experimental values as only solid material contributes to the experimentally determined values. The mean values per time step of the calculated G, V, and $\dot{T}$ were determined to allow comparison to the measured X-ray diffraction signals, which contain averaged information from the crystalline material in the interaction volume.

Next, the primary solidification phase was predicted utilizing the KGT model [15]. The KGT model predicts the dendrite growth kinetics for a given alloy at a fixed temperature gradient during directional solidification, accounting for non-equilibrium interface conditions during rapid solidification. The dendrite tip temperature can be calculated using this model, taking multicomponent thermodynamic and kinetic information as input. A higher dendrite tip temperature indicates a higher driving force to form for the respective phase. The KGT model was extended for multicomponent systems by Fukumoto and Kurz [17] and Babu et al. [8] and was utilized to predict the transition from δ-ferrite as the primary solid phase to γ during rapid solidification. More details of the implementation and input values for these calculations can be found in Chou et al. [20]. The utilized input parameters for the KGT model are listed in Table 2.

3. Results

3.1. Suppression of δ-ferrite during solidification

Fig. 4 shows the peak evolution before, during, and after laser scanning of the hot-work tool steel recorded at 40 000 Hz in reflection mode during printing with the MiniSLM. The positional relation of the laser and the X-ray beam in the MiniSLM is schematically illustrated in Fig. 4(a). In Fig. 4(b) and (c), the normalized diffraction intensities are depicted by colour (square root intensity colour bar). In these figures, the x-axis and y-axis values show the time and q-space, respectively. The magnitude of the scattering vector in q-space is obtained with $q = 4\pi/\lambda \times sin(\theta)$, where λ is the X-ray wavelength and θ is one half of the diffraction angle 2θ.

As shown in Fig. 4(b), the starting microstructure of the steel sample volume illuminated by X-rays was predominantly α'-martensite. When the laser approached the interaction volume, the α'-martensite peak positions slightly decreased before the martensite transformed to γ at ≈ -4 ms (Fig. 4(c)). Between -4 ms and 0 ms, the γ peak positions continuously increased, a signature of sample cooling, indicating that a laser scan of a neighbouring sample volume provided the required heat for the α' to γ transformation at -4 ms (Fig. 4(c), position=1). At 0 ms, the laser scanned through the X-ray interaction volume, and amorphous diffraction patterns were observed, characteristic of complete liquid within the melt pool (Fig. 4(c), position=2). During the next ≈ 5 ms, γ peaks appeared with increasing intensity, indicating solidification, and increasing peak position values, indicating cooling. At ≈ 5 ms, the laser returned to the X-ray interaction volume during scanning of the

subsequent track. During scanning of the subsequent track, the laser beam and X-ray interaction volume were not aligned anymore and the recorded XRD data included an amorphous signal from the melt as well as crystalline peaks from the solid material. Furthermore, between ≈ 5 ms and ≈ 10 ms, double γ peaks were observed at ≈ 57 nm^{-1} and ≈ 59 nm^{-1}. These double peaks imply the contribution of two γ regions to the signal within the X-ray interaction volume. The subsequent laser scan tracks resulted in a decaying cyclic behaviour of the peak positions until ≈ 20 ms. Afterwards, the microstructure in the X-ray interaction volume was predominantly γ until ≈ 60 ms, at which point an incomplete martensitic transformation from γ to α' was observed. In the following, only signal from conditions that exhibit solidification from completely liquid signal (Fig. 4(c), position=2) were evaluated to determine the solidification conditions.

In Fig. 5(a) and (b), the diffraction heat maps of the transmission mode measurement (AM-Replicator) and reflection mode measurement (MiniSLM) are shown focusing on the solidification after complete melting, respectively. At times before 0 ms, before the laser scans through the interaction volume, α' and γ peaks ($\{110\}_{\alpha'}$, $\{200\}_{\alpha'}$, $\{211\}_{\alpha'}$, $\{111\}_{\gamma}$, $\{200\}_{\gamma}$, $\{220\}_{\gamma}$) are observed and exhibit a decrease of q-spacing before they disappear when melted by the laser. After *time=0* ms, the primary solidification phase in the AM-Replicator is δ-ferrite ($\{110\}_{\delta}$, $\{200\}_{\delta}$, $\{211\}_{\delta}$) followed by γ. In contrast, the primary solidification phase in the MiniSLM is γ; δ-ferrite is not observed during solidification.

3.2. Thermal conditions

The thermal evolution during solidification is evaluated from the diffraction peak positions. In Fig. 5(b) and (c), the decreasing lattice parameters of γ obtained from the corresponding $\{111\}_{\gamma}$, $\{200\}_{\gamma}$, $\{220\}_{\gamma}$ peaks during solidification are plotted. The first γ mean lattice parameter observed in both setups is ≈ 3.71 Å. While in the AM-Replicator it takes ≈ 95 ms for the mean lattice parameter to decrease to 3.64 Å, in the MiniSLM the same mean lattice parameter decrease took only ≈ 1.85 ms. Assuming that only the thermal expansion contributes to the lattice parameter decrease, the change of the lattice parameter from 3.71 Å (≈ 1750 K) to 3.64 Å (≈ 885 K) is associated with a temperature decrease of approximately 865 K.

From the change in lattice parameter, the measured cooling rates (Eq. (3)), together with the calculated cooling rates obtained from the Rosenthal equation, are plotted in Fig. 5(d) and (e). The initial cooling rate observed in the AM-Replicator is approximately 21 200 K/s, whereas the initial cooling rate observed in the MiniSLM is approximately two orders of magnitude higher (1,500,000 K/s). Moreover, the calculated cooling rates are in good agreement with the estimated cooling rates from experiments.

Table 3 shows the mean (± range) of the initial cooling rate $\dot{T}$, thermal gradient G, and solidification velocity V within the X-ray interaction volume analytically evaluated with the Rosenthal equation for both setups during the first millisecond of solidification. As expected, the conditions generated by the AM-Replicator with a laser power of 218.4 W and a scan speed of 0.05 m/s result in significantly lower $\dot{T}$, G, and V compared to the conditions generated by the MiniSLM with a laser power of 300 W and a scanning speed of 0.6 m/s.

3.3. Solidification mode

The tip temperatures of δ-ferrite and γ are predicted by applying the extended KGT model to evaluate the primary solidification phase under AM conditions. Fig. 6 includes these calculated dendritic tip temperatures as a function of the solidification velocity of the γ phase (red lines) and the δ-ferrite phase (blue lines) for thermal gradients of 10^5 K/m, 10^6 K/m, 10^7 K/m and 10^8 K/m. These include the predicted thermal gradient ranges during the initial solidification at AM-replicator and at MiniSLM conditions, respectively (see Table 3). In Fig. 6 the range of the solidification velocities in both setups is indicated by vertical bands (AM-Replicator: blue, MiniSLM: red). At solidification velocities below ≈ 0.1 m/s, the tip temperature of δ-ferrite is higher than the tip temperature of γ, indicating that δ-ferrite will be the primary solidification phase at these conditions. At solidification velocities higher than ≈ 0.2 m/s, the tip temperature of γ is higher than the tip temperature of δ-ferrite, suggesting that at these conditions, γ is the primary solidification phase. The vertical dotted and dashed lines highlight the solidification velocity calculated (with the Rosenthal equation) for the conditions generated by the AM-Replicator and the MiniSLM, respectively. At the AM-Replicator conditions, the KGT model predicts δ-ferrite to be the primary solidification phase, while the primary solidification phase under MiniSLM conditions is predicted to be γ, in good agreement with the experimental observations.

4. Discussion

The solidification mode in steels is dependent on the thermal conditions and the composition [57]. Our previous work showed no indications that δ-ferrite had formed during L-PBF of a hot-work tool steel based on post-process microstructure characterization of the as-built microstructure and computational modelling predicted that suppression of the δ-ferrite formation during solidification at high solidification velocities is expected [20]. In this work, we observe the change in the solidification mode of this hot-work tool steel with *in situ* XRD at AM conditions, thereby providing evidence for the predictions by the solidification tip temperature model.

The solidification during AM, and specifically during L-PBF, is governed by the fast cooling of a comparably small melt pool after rapid laser scanning [1]. During the MiniSLM experiments, we obtained an initial $\dot{T}$ of $1.5 \bullet 10^6$ K/s. This value agrees with previously reported cooling rates typical for L-PBF [24,58,59], and it is reasoned that the measurements recorded in the MiniSLM are representative of L-PBF conditions. The solidification mode observed in the MiniSLM XRD data is primary austenite and the formation of δ-ferrite appears to be suppressed (Fig. 5(b)). However, with the measurement in reflection mode, data from the upper part of the melt pool is obtained. In L-PBF, this upper part of the melt pool is at least partly remelted during printing of the subsequent layer. Therefore, the solidification at the bottom part of the melt pool will be decisive for the resulting microstructure [60,61]. Even though, we report the solidification events from the upper part of the melt pool, and the accuracy of the reported results is limited, we assume that the measured values are within a relevant range to allow for studies of the solidification mode in L-PBF. Neither during solidification from the melt pool nor in the previous and subsequent intrinsic heat treatment induced by laser scanning of neighbouring paths is δ-ferrite observed (Fig. 4). Furthermore, measurements in the AM-Replicator allowed for solidification conditions at two orders of magnitude smaller $\dot{T}$ ($2.12 \bullet 10^4$ K/s) to be studied. In these measurements, the solidification mode is primary δ-ferrite.

Utilizing both experimental setups allowed us to study a range of solidification conditions and to observe the different solidification modes *in situ* (Fig. 5(a) and (b)). It is emphasized that the observed solidification modes cannot directly be investigated with *ex situ* methods, as solid-state phase transformations will occur during cooling down to room temperature. Nevertheless, the cooling rates determined from the peak positions of XRD data inherit several uncertainties [40,41,44,62]. First, the diffraction signal is obtained from the interaction volume of the X-ray beam with the sample [40,41,44,62]. Therefore, the peak positions are averaged over the melt pool with a temperature gradient G (Fig. 5). Second, the peak positions of the γ peaks are used for the calculation. Thereby, $\dot{T}$ is obtained for the solid-fraction of the melt pool, neglecting $\dot{T}$ of the liquid, as well as neglecting $\dot{T}$ of δ-ferrite in the AM-Replicator measurement. Third, to calculate $\dot{T}$ from the measured peak positions in Eq. (3), the *CTE* is considered constant [40,41], while *CTE* is a temperature dependent parameter (compare Fig. 2). As the

change of the *CTE* from 1750 K to 1400 K is less than 1%, this is neglected. Fourth, the effect of residual stress and strain is neglected given solidification from liquid and the high $\dot{T}$ [40,44]. Lastly, the effect of compositional variations on the peak position is also disregarded given the fast timescale [40]. In summary, it is approximated that during initial solidification with high $\dot{T}$ from the melt, only thermal contractions govern the lattice parameter change [40,44]. This approximation is sensitive to the probed location. In Fig. 4 at ≈ 4 ms the double γ peaks are observed after melting of a track. The double peaks are accounted to signal within the X-ray interaction volume arising from different zones of the melt pool and heat-affected zone (HAZ). Schmeiser et al. [38] describe the varying stress fields in the HAZ that are caused by very high heating and cooling rates in L-PBF. In this study, only solidification events that exhibited solidification from complete liquid X-ray interaction volume are therefore studied.

G and *V* during the experiments are determined by fitting an analytical solution (Rosenthal equation) to the experimental $\dot{T}$ values (Fig. 5(e) and (f)). Even though this solution disregards heat convection and radiation, it has been shown that the Rosenthal equation can provide reasonable thermal conditions, which can be applied to predict the solidification microstructure in L-PBF [63]. The obtained *G* and *V* values (Table 3) are applied to map the solidification conditions in the predicted solidification mode space (Fig. 6), which was calculated using the KGT model [15] for the investigated composition. Despite simplifications, the predictions obtained by the KGT model are in line with experimental observations and provide insights into the difference in the solidification mode in the L-PBF process measurements purely based on the thermal conditions experienced by the solidifying material and its composition. The presented results indicate that the KGT model can be applied to predict the solidification sequence at rapid solidification conditions during L-PBF based on multicomponent thermodynamic and kinetic information. Predicting the solidification mode is important to understand the process-microstructure-property relationship of steels processed by L-PBF. The solidification mode and the resulting solidification structure influence the solid-state phase transformations during cooling and intrinsic heat treatment, and hence, the resulting microstructure. With this knowledge, e.g., the process-induced cracking, which is observed in L-PBF processed steels and dependent on the solidification conditions can be addressed [17,57,64].

Further understanding of the process-microstructure-property relations could be obtained by investigating the segregation and stresses at rapid solidification conditions. In the presented work, we show how the thermal conditions during processing can be linked to the occurring solidification mode in L-PBF of hot-work tool steel, which is an important step towards accessing the full design space of additive manufacturing of metals.

5. Conclusions

The presented results show that *in situ* synchrotron X-ray diffraction can be used to study the solidification in the melt pool at L-PBF conditions and to investigate the thermal conditions during solidification. Two experimental setups were used to access a range of solidification conditions, allowing for the observation of two solidification modes in a hot-work tool steel: primary δ-ferrite and primary austenite.

Moreover, the thermal conditions during solidification were inferred from XRD data and could be linked to a model for rapid solidification enabling the model validation and, in turn, allowing for the solidification mode in L-PBF to be predicted. These findings can enable parameter development for the AM processes and benefit the development of alloys specifically for AM with computational models.

Data statement

The datasets analysed in the current study are available from the corresponding author on reasonable request.

Declaration of Competing Interest

The authors declare that they have no known competing financial interests or personal relationships that could have appeared to influence the work reported in this paper.

Acknowledgments

This work was performed with financial support from the Swedish Governmental Agency for Innovation Systems (Vinnova) and the National Research Council (VR) via the projects *In-situ X-ray diffraction study of additive manufacturing to aid in tool steel development* (2019-0527) and *Real-time tracking of electron-beam AM* (2019-06068). This research used resources of the Advanced Photon Source, a U.S. Department of Energy (DOE) Office of Science user facility operated for the DOE Office of Science by Argonne National Laboratory under Contract No. DE-AC02-06CH11357. LC acknowledges the support from the US National Science Foundation under grants CMMI – 2011354 and CMMI – 2002840. GL also acknowledges support from Vinnova, Formas and Energimyndigheten via LIGHTer Academy.

Appendices

A. *Adjustment for layer shrinkage*

The reflection mode XRD measurements are sensitive to height changes of the measurement position on the sample, as those will change the sample-detector distance for which the measurement is calibrated. Due to the layer-by-layer build-up of the sample, laser scanning, thermal expansion and gravity [65] during the reflection mode measurements, the recorded signal positions can be shifted (Fig. 7). To account for the shift, the sample-detector distance during the measurements is adjusted. Therefore, the as-built bcc lattice parameter of the sample material at RT (a_{bcc} = 2.874Å) obtained from the measurements in the AM-Replicator before melting of the sample is utilized to calculate the expected diffraction angles at the conditions during the reflection measurements with Bragg's law for cubic systems (X-ray wavelength: λ = 17.2 keV/0.7208 Å):

$$\theta_1 = \sin^{-1}\left(\frac{\lambda}{2\left(\frac{a_{bcc}}{\sqrt{h^2+k^2+l^2}}\right)}\right) \tag{A1}$$

The positions of the recorded bcc peaks on the detector (*P*) are calculated with the sample detector distance of the initial calibration (SD_2), the recorded peak positions $\theta_{2(recorded)}$ and the detector tilt (31.01°):

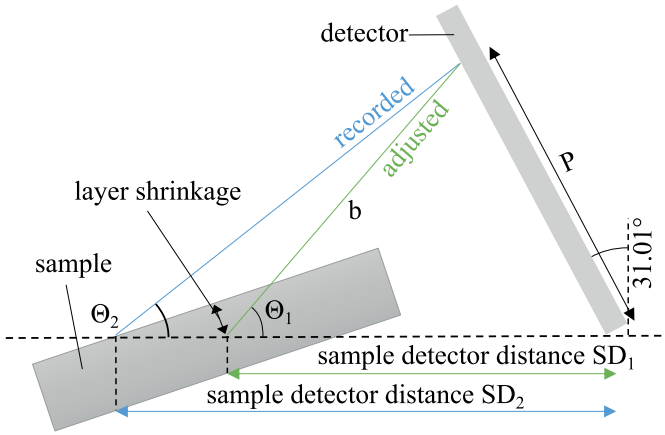

Fig. 7. Schematic showing the signal position on the detector and the resulting related angular position with and without accounting for the layer shrinkage.

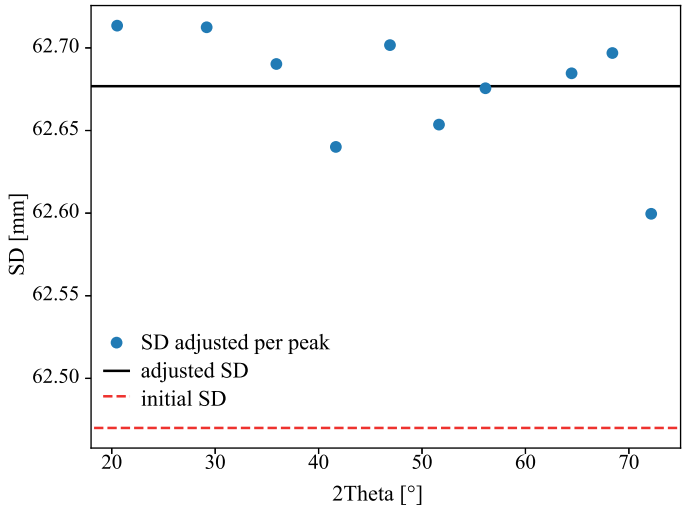

Fig. 8. Evaluated sample detector distances from the respective peaks (blue dots), mean sample detector distance (black line) and initial sample detector distance (red dashed line). (For interpretation of the references to colour in this figure legend, the reader is referred to the web version of this article.).

$$P = \frac{SD_2 \cdot sin\left(\left(2 \cdot \theta_{2(recorded)}\right)\right)}{sin\left(90^{\circ} + detector\ tilt - 2 \cdot \theta_{2(recorded)}\right)} \tag{A2}$$

The peak positions on the detector (P) are used to calculate the detector distance during the measurement (SD_1):

$$SD_1 = \frac{P \cdot sin(90^{\circ} + detector\ tilt - 2 \cdot \theta_1)}{sin((2 \cdot \theta_1)} \tag{A3}$$

Evaluated detector distances from a reflection mode measurement are shown in Fig. 8.

With the obtained detector distance, every angle coordinate point in the integrated data is corrected by applying Eq. (A2) to evaluate the correlating position on the detector and the corrected angle with Eqs. (A4) and (A5):

$$b = P^2 + SD_1^2 - 2 \cdot P \cdot SD_1 \cdot \cos(90 - detector\_tilt) \tag{A4}$$

$$\theta_{corrected} = \arccos\left(\frac{b^2 + SD_1^2 - P^2}{2 \cdot b \cdot c}\right) \tag{A5}$$

The accuracy of this method is limited as the lattice parameter at room temperature is also influenced by stresses in the sample. However, the adjustment increases the comparability of measurements from different setups. In Fig. 9, the initially recorded data and the adjusted data are shown. The calculated bcc peaks of the sample material for the utilized X-ray energy are indicated.

B. XRD data and fit

Fig. 10 shows examples of the recorded and normalized data after laser scanning, the fitted model to the data and the fitted models residuals. In Fig. 10(a) and (c), the AM-Replicator transmission mode data and in Fig. 10(b) and (d), the MiniSLM reflection mode data are plotted. Here, the significantly different temporal resolutions in both experiments should be noted. In measurements with the AM-Replicator, a frame rate of 250 Hz and

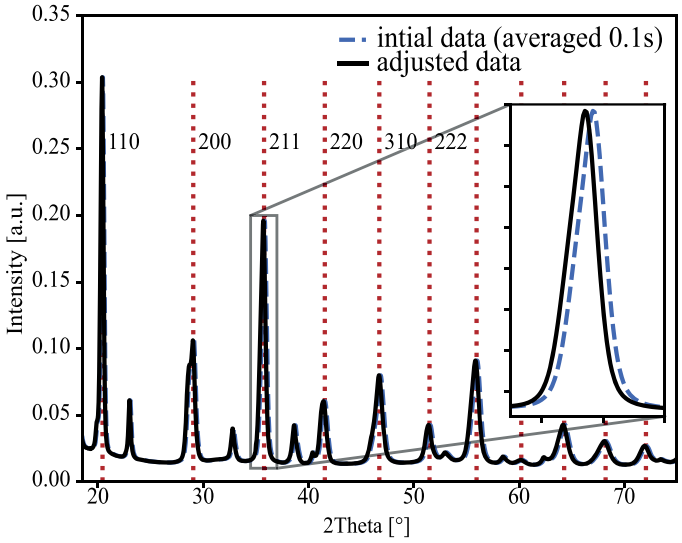

Fig. 9. The recorded data of a reflection measurement, initial (blue dashed line), adjusted for shrinkage (black line) and calculated peak angles (red dotted lines). (For interpretation of the references to colour in this figure legend, the reader is referred to the web version of this article.).

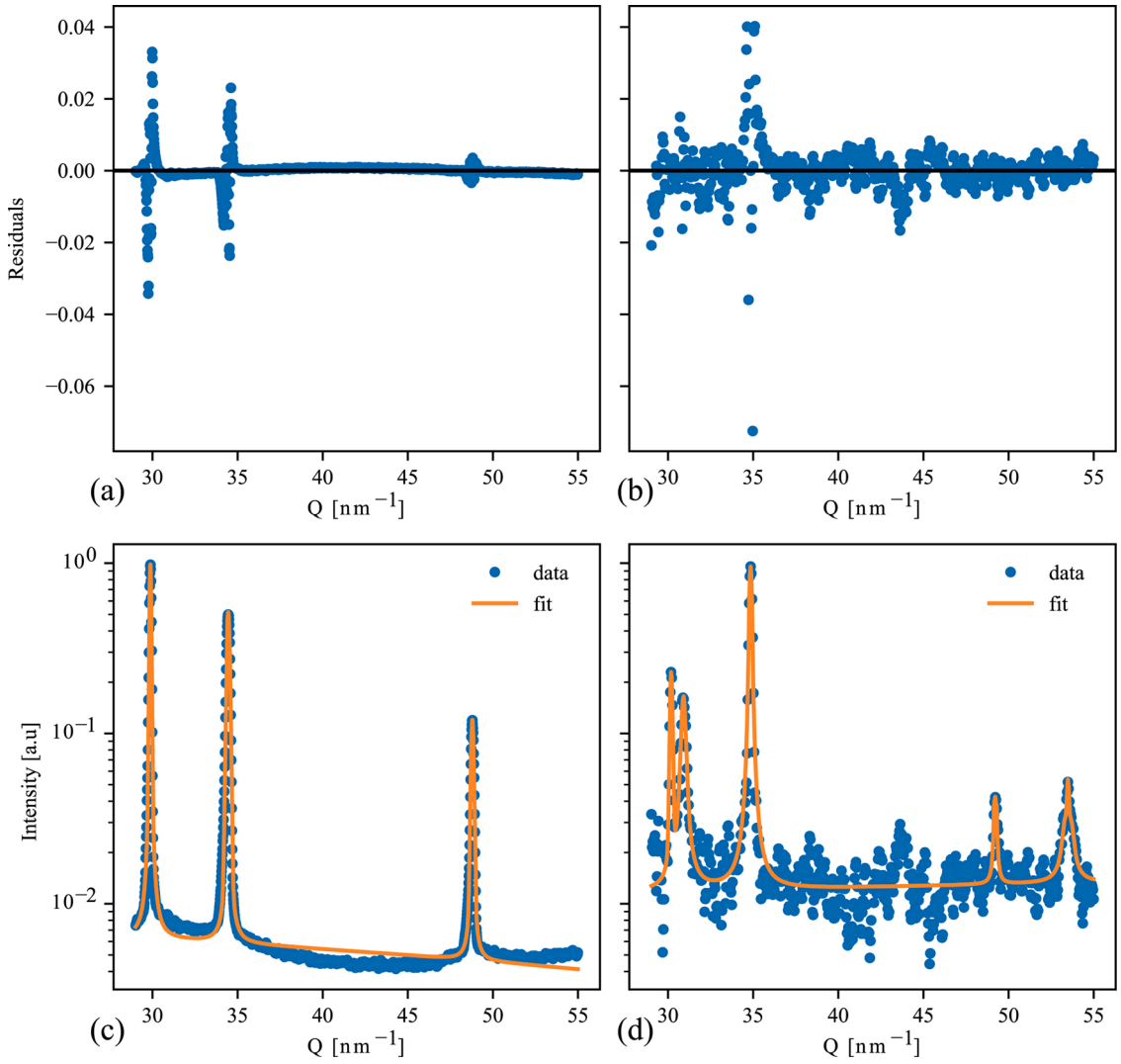

Fig. 10. XRD data quality; (c) AM-Replicator, XRD line profile and peak fit (d) MiniSLM, XRD line profile and peak fit. (a) AM-Replicator, residuals (b) MiniSLM, residuals.

an exposure time of 3 ms per frame at 61.338 keV is applied. These measurement settings result in a lower signal-to-noise ratio compared to the measurement settings utilized in the MiniSLM (frame rate: 20 000 Hz or 40 000 Hz, exposure time: 45 μs or 20 μs, beam energy: 17.2 keV) (compare Fig. 10(c) and (d)).

References

[1] T. DebRoy, H.L. Wei, J.S. Zuback, T. Mukherjee, J.W. Elmer, J.O. Milewski, A. M. Beese, A. Wilson-Heid, A. De, W. Zhang, Additive manufacturing of metallic components – process, structure and properties, Prog. Mater. Sci. 92 (2018) 112–224.

[2] H.L. Wei, T. Mukherjee, W. Zhang, J.S. Zuback, G.L. Knapp, A. De, T. DebRoy, Mechanistic models for additive manufacturing of metallic components, Prog. Mater. Sci. 116 (2021), 100703.

[3] P. Bajaj, A. Hariharan, A. Kini, P. Kürnsteiner, D. Raabe, E.A. Jägle, Steels in additive manufacturing: a review of their microstructure and properties, Mater. Sci. Eng. A. 772 (2020), 138633.

[4] J.O. Milewski, Additive manufacturing of metals, (Vol. 258,, Springer International Publishing AG, Cham, Switzerland, 2017, pp. 134–157.

[5] W. Kurz, D.J. Fisher, R. Trivedi, Progress in modelling solidification microstructures in metals and alloys: dendrites and cells from 1700 to 2000, Int. Mater. Rev. 64 (2019) 311–354.

[6] W. Kurz, M. Rappaz, R. Trivedi, Progress in modelling solidification microstructures in metals and alloys. Part II: dendrites from 2001 to 2018, Int. Mater. Rev. 66 (2021) 30–76.

[7] N. Provatas, T. Pinomaa, N. Ofori-Opoku, Quantitative Phase Field Modelling of Solidification, CRC Press, Boca Raton, 2021.

[8] S.S. Babu, J.W. Elmer, J.M. Vitek, S.A. David, Time-resolved X-ray diffraction investigation of primary weld solidification in Fe-C-Al-Mn steel welds, Acta Mater. 50 (2002) 4763–4781.

[9] T. Hashimoto, H. Terasaki, Y. Komizo, Effect of tip velocity on weld solidification process of hot-work tool steel, Weld. Int. 23 (2009) 431–438.

[10] S. Karagadde, C.L.A. Leung, P.D. Lee, Progress on *in situ* and operando x-ray imaging of solidification processes, Materials 14 (2021) 2374 (Basel).

[11] W. Kurz, Solidification microstructure-processing maps: theory and application, Adv. Eng. Mater. 3 (2001) 443–452.

[12] M.M. Kirka, P. Nandwana, Y. Lee, R.R. Dehoff, Solidification and solid-state transformation sciences in metals additive manufacturing, Scr. Mater. 135 (2017) 130–134.

[13] T.M. Pollock, A.J. Clarke, S.S. Babu, Design and tailoring of alloys for additive manufacturing, Metall. Mater. Trans. A Phys. Metall. Mater. Sci. 51 (2020) 6000–6019.

[14] W.J. Boettinger, The solidification of multicomponent alloys, J. Ph. Equilibria Diffus. 37 (2016) 4–18.

[15] W. Kurz, B. Giovanola, R. Trivedi, Theory of microstructural development during rapid solidification, Acta Metall. 34 (1986) 823–830.

[16] T. Hashimoto, H. Terasaki, Y. Komizo, Effect of solidification velocity on weld solidification process of alloy tool steel, Sci. Technol. Weld. Join. 13 (2008) 409–414.

[17] S. Fukumoto, W. Kurz, Prediction of the δ to γ transition in austenitic stainless steels during laser treatment, ISIJ Int. 38 (1998) 71–77.

[18] L. Wu, S. Das, W. Gridin, S. Leuders, M. Kahlert, M. Vollmer, T. Niendorf, Hot work tool steel processed by laser powder bed fusion: a review on most relevant influencing factors, Adv. Eng. Mater. 23 (2021), 2100049.

[19] P. Mayr, C. Schlacher, J.A. Siefert, J.D. Parker, Microstructural features, mechanical properties and high temperature failures of ferritic to ferritic dissimilar welds, Int. Mater. Rev. 64 (2019) 1–26.

[20] C.Y. Chou, N.H. Pettersson, A. Durga, F. Zhang, C. Oikonomou, A. Borgenstam, J. Odqvist, G. Lindwall, Influence of solidification structure on austenite to martensite transformation in additively manufactured hot-work tool steels, Acta Mater. 215 (2021), 117044.

[21] N.D. Parab, C. Zhao, R. Cunningham, L.I. Escano, K. Fezzaa, W. Everhart, A. D. Rollett, L. Chen, T. Sun, Ultrafast X-ray imaging of laser–metal additive manufacturing processes, J. Synchrotron Radiat. 25 (2018) 1467–1477.

[22] A.A. Martin, N.P. Calta, J.A. Hammons, S.A. Khairallah, M.H. Nielsen, R. M. Shuttlesworth, N. Sinclair, M.J. Matthews, J.R. Jeffries, T.M. Willey, J.R.I. Lee, Ultrafast dynamics of laser-metal interactions in additive manufacturing alloys captured by *in situ* X-ray imaging, Mater. Today Adv. 1 (2019), 100002.

[23] C. Ioannidou, H.H. König, N. Semjatov, U. Ackelid, P. Staron, C. Körner, P. Hedström, G. Lindwall, *In-situ* synchrotron X-ray analysis of metal additive manufacturing: current state, opportunities and challenges, Mater. Des. 219 (2022), 110790.

[24] C. Zhao, K. Fezzaa, R.W. Cunningham, H. Wen, F. De Carlo, L. Chen, A.D. Rollett, T. Sun, Real-time monitoring of laser powder bed fusion process using high-speed X-ray imaging and diffraction, Sci. Rep. 7 (2017) 1–11.

[25] E. Uhlmann, E. Krohmer, F. Schmeiser, N. Schell, W. Reimers, A laser powder bed fusion system for *in situ* x-ray diffraction with high-energy synchrotron radiation, Rev. Sci. Instrum. 91 (2020), 075104.

[26] C.L.A. Leung, S. Marussi, R.C. Atwood, M. Towrie, P.J. Withers, P.D. Lee, *In situ* X-ray imaging of defect and molten pool dynamics in laser additive manufacturing, Nat. Commun. 9 (2018) 1–9.

[27] S. Hocine, S. Van Petegem, U. Frommherz, G. Tinti, N. Casati, D. Grolimund, H. Van Swygenhoven, A miniaturized selective laser melting device for operando X-ray diffraction studies, Addit. Manuf. 34 (2020), 101194.

[28] N.P. Calta, J. Wang, A.M. Kiss, A.A. Martin, P.J. Depond, G.M. Guss, V. Thampy, A. Y. Fong, J.N. Weker, K.H. Stone, C.J. Tassone, M.J. Kramer, M.F. Toney, A. Van Buuren, M.J. Matthews, An instrument for *in situ* time-resolved X-ray imaging and diffraction of laser powder bed fusion additive manufacturing processes, Rev. Sci. Instrum. 89 (2018), 055101.

[29] Chen, Y., Clark, S. J., Sinclair, L., Leung, C. L. A., Marussi, S., Connolley, T., ... & Lee, P. D. (2020). In situ and operando X-ray imaging of directed energy deposition additive manufacturing. *arXiv preprint arXiv:2006.09087*.

[30] J. Epp, J. Dong, H. Meyer, A. Bohlen, Analysis of cyclic phase transformations during additive manufacturing of hardenable tool steel by *in-situ* X-ray diffraction experiments, Scr. Mater. 177 (2020) 27–31.

[31] S.J Wolff, S Webster, N.D Parab, B Aronson, B Gould, A Greco, T Sun, *In-situ* observations of directed energy deposition additive manufacturing using high-speed X-ray imaging, JOM 73 (2020) 189–200.

[32] Q Guo, C Zhao, M Qu, L Xiong, S.M.H Hojjatzadeh, L.I Escano, N.D Parab, K Fezzaa, T Sun, L Chen, *In-situ* full-field mapping of melt flow dynamics in laser metal additive manufacturing, Addit. Manuf. 31 (2020), 100939.

[33] Y. Huang, T.G. Fleming, S.J. Clark, S. Marussi, K. Fezzaa, J. Thiyagalingam, C.L. A. Leung, P.D. Lee, Keyhole fluctuation and pore formation mechanisms during laser powder bed fusion additive manufacturing, Nat. Commun. 13 (2022) 1170.

[34] A.A. Martin, N.P. Calta, S.A. Khairallah, J. Wang, P.J. Depond, A.Y. Fong, V. Thampy, G.M. Guss, A.M. Kiss, K.H. Stone, C.J. Tassone, J.N. Weker, M. F. Toney, T. van Buuren, M.J. Matthews, Dynamics of pore formation during laser powder bed fusion additive manufacturing, Nat. Commun. 10 (2019) 1–10.

[35] N. Kouraytem, P.J.J. Chiang, R. Jiang, C. Kantzos, J. Pauza, R. Cunningham, Z. Wu, G. Tang, N. Parab, C. Zhao, K. Fezzaa, T. Sun, A.D. Rollett, Solidification crack propagation and morphology dependence on processing parameters in AA6061 from ultra-high-speed x-ray visualization, Addit. Manuf. 42 (2021), 101959.

[36] H. Ghasemi-Tabasi, C. de Formanoir, S. Van Petegem, J. Jhabvala, S. Hocine, E. Boillat, N. Sohrabi, F. Marone, D. Grolimund, H. Van Swygenhoven, R.E. Logé, Direct observation of crack formation mechanisms with operando laser powder bed fusion X-ray imaging, Addit. Manuf. 51 (2022), 102619.

[37] S.A. Oh, R.E. Lim, J.W. Aroh, A.C. Chuang, B.J. Gould, B. Amin-Ahmadi, A. D. Rollett, High speed synchrotron X-ray diffraction experiments resolve microstructure and phase transformation in laser processed Ti-6Al-4V, Materials Research Letters 9 (10) (2021) 429–436.

[38] F. Schmeiser, E. Krohmer, N. Schell, E. Uhlmann, W. Reimers, Experimental observation of stress formation during selective laser melting using *in situ* X-ray diffraction, Addit. Manuf. 32 (2020), 101028.

[39] F. Schmeiser, E. Krohmer, N. Schell, E. Uhlmann, W. Reimers, Internal stress evolution and subsurface phase transformation in titanium parts manufactured by laser powder bed fusion—an *in situ* X-ray diffraction study, Adv. Eng. Mater. 23 (2021), 2001502.

[40] V. Thampy, A.Y. Fong, N.P. Calta, J. Wang, A.A. Martin, P.J. Depond, A.M. Kiss, G. Guss, Q. Xing, R.T. Ott, A. van Buuren, M.F. Toney, J.N. Weker, M.J. Kramer, M. J. Matthews, C.J. Tassone, K.H. Stone, Subsurface cooling rates and microstructural response during laser based metal additive manufacturing, Sci. Rep. 10 (2020) 1981.

[41] J.A. Glerum, S. Hocine, C. Sin, T. Chang, C. Kenel, S. Van Petegem, N. Casati, D. F. Sanchez, H. Van Swygenhoven, D.C. Dunand, Operando X-ray diffraction study of thermal and phase evolution during laser powder bed fusion of Al-Sc-Zr elemental powder blends, Addit. Manuf. 55 (2022), 102806.

[42] J.O. Andersson, T. Helander, L. Höglund, P. Shi, B. Sundman, Thermo-Calc & DICTRA, computational tools for materials science, Calphad 26 (2002) 273–312.

[43] Thermo-Calc software TCFE steels/Fe-alloys database version 11, (2021).

[44] S. Hocine, H. Van Swygenhoven, S. Van Petegem, C.S.T. Chang, T. Maimaitiyili, G. Tinti, D. Ferreira Sanchez, D. Grolimund, N. Casati, Operando X-ray diffraction during laser 3D printing, Mater. Today 34 (2020) 30–40.

[45] G. Tinti, A. Bergamaschi, S. Cartier, R. Dinapoli, D. Greiffenberg, I. Johnson, J. H. Jungmann-Smith, D. Mezza, A. Mozzanica, B. Schmitt, X. Shi, Performance of the EIGER single photon counting detector, J. Instrum. 10 (2015) C03011. C03011.

[46] J. Liu, R.E. Saw, Y.H. Kiang, Calculation of effective penetration depth in X-ray diffraction for pharmaceutical solids, J. Pharm. Sci. 99 (2010) 3807–3814.

[47] V.P. Singh, N.M. Badiger, Study of mass attenuation coefficients, effective atomic numbers and electron densities of carbon steel and stainless steels, Radioprotection 48 (2013) 431–443.

[48] A.P. Hammersley, FIT2D: A multi-purpose data reduction, analysis and visualization program, J. Appl. Crystallogr. 49 (2016) 646–652.

[49] G. Ashiotis, A. Deschildre, Z. Nawaz, J.P. Wright, D. Karkoulis, F.E. Picca, J. Kieffer, The fast azimuthal integration Python library: pyFAI, J. Appl. Crystallogr. 48 (2015) 510–519.

[50] Newville, M., Stensitzki, T., Allen, D. B., Rawlik, M., Ingargiola, A., & Nelson, A. (2016). LMFIT: Non-linear least-square minimization and curve-fitting for Python. *Astrophysics Source Code Library*, ascl-1606.

[51] D. Rosenthal, Mathematical theory of heat distribution during welding and cutting, Weld. J. 20 (1941) 220–234.

[52] A. Plotkowski, M.M. Kirka, S.S. Babu, Verification and validation of a rapid heat transfer calculation methodology for transient melt pool solidification conditions in powder bed metal additive manufacturing, Addit. Manuf. 18 (2017) 256–268.

[53] S. Bontha, N.W. Klingbeil, P.A. Kobryn, H.L. Fraser, Thermal process maps for predicting solidification microstructure in laser fabrication of thin-wall structures, J. Mater. Process. Technol. 178 (2006) 135–142.
[54] R. Indhu, V. Vivek, L. Sarathkumar, A. Bharatish, S. Soundarapandian, Overview of laser absorptivity measurement techniques for material processing, Lasers Manuf. Mater. Process. 5 (2018) 458–481.
[55] Uddeholms AB, Uddeholm dievar®, https://www.uddeholm.com/. (2017).
[56] M.J. Aziz, Model for solute redistribution during rapid solidification, J. Appl. Phys. 53 (1982) 1158–1168.
[57] J.W. Elmer, S.M. Allen, T.W. Eagar, Microstructural development during solidification of stainless steel alloys, Metall. Trans. A 20 (1989) 2117–2131.
[58] P.A. Hooper, Melt pool temperature and cooling rates in laser powder bed fusion, Addit. Manuf. 22 (2018) 548–559.
[59] Y. Li, D. Gu, Parametric analysis of thermal behavior during selective laser melting additive manufacturing of aluminum alloy powder, Mater. Des. 63 (2014) 856–867.
[60] F. Schmeiser, E. Krohmer, C. Wagner, N. Schell, E. Uhlmann, W. Reimers, *In situ* microstructure analysis of Inconel 625 during laser powder bed fusion, J. Mater. Sci. 57 (2022) 9663–9677.
[61] H.E. Sabzi, N.T. Aboulkhair, X. Liang, X.H. Li, M. Simonelli, H. Fu, P.E.J. Rivera-Díaz-del-Castillo, Grain refinement in laser powder bed fusion: the influence of dynamic recrystallization and recovery, Mater. Des. 196 (2020), 109181.
[62] N.P. Calta, V. Thampy, D.R.C. Lee, A.A. Martin, R. Ganeriwala, J. Wang, P. J. Depond, T.T. Roehling, A.Y. Fong, A.M. Kiss, C.J. Tassone, K.H. Stone, J. N. Weker, M.F. Toney, A.W. Van Buuren, M.J. Matthews, Cooling dynamics of two titanium alloys during laser powder bed fusion probed with *in situ* X-ray imaging and diffraction, Mater. Des. 195 (2020), 108987.
[63] P. Promoppatum, S.C. Yao, P.C. Pistorius, A.D. Rollett, A comprehensive comparison of the analytical and numerical prediction of the thermal history and solidification microstructure of inconel 718 products made by laser powder-bed fusion, Engineering 3 (2017) 685–694.
[64] J. Krell, A. Röttger, K. Geenen, W. Theisen, General investigations on processing tool steel X40CrMoV5-1 with selective laser melting, J. Mater. Process. Technol. 255 (2018) 679–688.
[65] C. Körner, A. Bauereiß, E. Attar, Fundamental consolidation mechanisms during selective beam melting of powders, Model. Simul. Mater. Sci. Eng. 21 (2013), 085011.